Article

Fluorine Translational Anion Dynamics in Nanocrystalline Ceramics: SrF_2-YF_3 Solid Solutions

Stefan Breuer [1]*, Bernhard Stanje [1], Veronika Pregartner [1], Sarah Lunghammer [1], Ilie Hanzu [1,2] and Martin Wilkening [1,2,†]

[1] Christian Doppler Laboratory for Lithium Batteries, and Institute for Chemistry and Technology of Materials, Graz University of Technology (NAWI Graz), Stremayrgasse 9, 8010 Graz, Austria
[2] Alistore-ERI European Research Institute, 33 rue Saint Leu, 80039 Amiens, France; wilkening@tugraz.at
* Correspondence: breuer@tugraz.at
† See also for correspondence: wilkening@tugraz.at; Tel.: +43-316-873-32330

Abstract: Nanostructured materials have already become an integral part of our daily life. In many applications ion mobility decisively affects the performance of, *e.g.*, batteries and sensors. Nanocrystalline ceramics often exhibit enhanced transport properties due to their heterogeneous structure showing crystalline (defect-rich) grains and disordered interfacial regions. In particular, anion conductivity in nonstructural binary fluorides easily exceeds that of their coarse-grained counterparts. To further increase ion dynamics aliovalent substitution is a practical method to influence the number of (i) defect sites and (ii) the charge carrier density. Here, we used high energy-ball milling to incorporate Y^{3+} ions into the cubic structure of SrF_2. As compared to pure nanocrystalline SrF_2 the ionic conductivity of $Sr_{1-x}Y_xF_{2+x}$ with $x = 0.3$ increased by 4 orders of magnitude reaching 0.8×10^{-5} S cm^{-1} at 450 K. We discuss the effect of YF_3 incorporation on conductivities isotherms determined by both activation energies and Arrhenius pre-factors. The enhancement seen is explained by size mismatch of the cations involved, which are forced to form a cubic crystal structure with extra F anions if x is kept smaller than 0.5.

Keywords: nanocrystalline ceramics; binary fluorides, ionic conductivity; ball milling; cation mixing; aliovalent substitution

1. Introduction

Nanostructured materials assume a variety of functions in quite different applications and devices of our daily life. Considering nanocrystalline ionic conductors [1–4], a range of studies report on enhanced anion and cation dynamics [5,6]. Structural disorder and defects [7–9], lattice mismatch [10–12] as well as size effects [13–17], which results in extended space charge regions, are used to explain the properties of nanocrystalline compounds. Especially for nano-engineered systems, which were prepared by bottom-up procedures, such as gas condensation or epitaxial methods [18,19], space charge regions lead to non-trivial effects that may enhance ion transport. This effect has not only been shown for the pioneering prototype system BaF_2-CaF_3 [18] but also, quite recently, for nanoscopic, grain-boundary engineered SrF_2-LaF_3 heterolayers [20].

If prepared via a top-down approach such as ball milling [7,21], the nanocrystalline material obtained is anticipated to consist of nm-sized crystals surrounded by structurally disordered regions [5,22]. In particular, this structural model helped rationalize ion dynamics in oxides [7]. For fluorides amorphous regions are present to a much lesser extent [23,24]. High-energy ball milling also increases the density of defects in the interior of the nanograins [9,24]. Starting with binary fluorides, such as nanocrystalline BaF_2, whose F anion conductivity exceeds that of BaF_2 monocrystals by some orders of magnitude [11], iso- and aliovalent substitution of the metal cations drastically improves ion transport [10,25]. As an example, in the nanocrystalline solid solutions $Me_{1-x}Sr_xF_2$ (Me = Ca, Ba) the ionic conductivity passes through a maximum at intermediate values of x while the corresponding

Preprints (www.preprints.org) | NOT PEER-REVIEWED | Posted: 25 January 2018 doi:10.20944/preprints201801.0234.v1

Peer-reviewed version available at Crystals 2018, 8, 122; doi:10.3390/cryst8030122

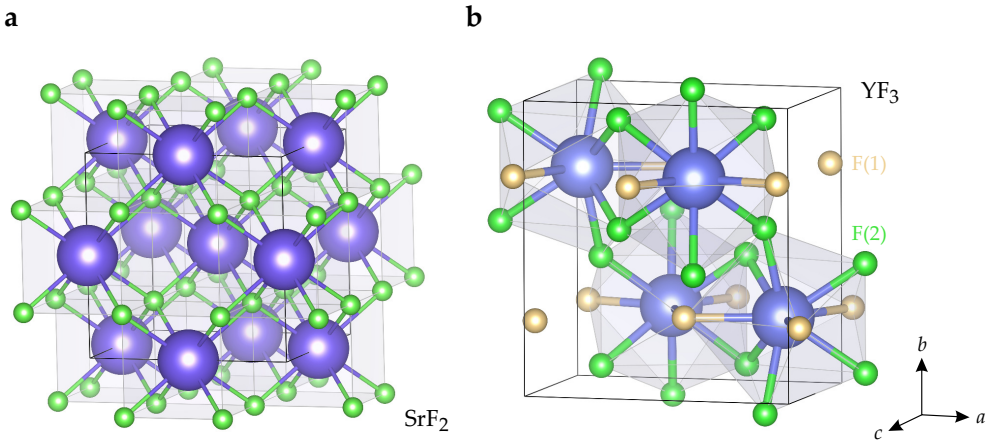

Figure 1. (**a**) Crystal structure ($Fd\bar{3}m$) of cubic SrF_2 with the Sr^{+2} ions (spheres in light blue, ionic radius 0.99 Å) occupying the 4*b* positions coordinated by eight fluorine anions residing on 8*c*. In (**b**) the crystal structure orthorhombic of YF_3 (*Pnma*) is shown; the trivalent Y^{3+} ions (light blue spheres, ionic radius 0.90 Å) occupy the 4*c* sites, two further crystallographically inequivalent F sites exist which are filled by the F anions F(1) and F (2).

activation energy shows a minimum, the same holds for $Ba_{1-x}Ca_xF_2$ [10]. Although the original cubic crystal structure remains untouched for the mixed systems, strain and defects resulting from mixing sensitively affects F anion dynamics [10,11,26]. Metastable $Ba_{1-x}Ca_xF_2$, however, cannot be prepared via solid state synthesis; instead, it is only accessible by high-energy ball milling that forces the cations ions, substantially differing in size, to form a solid solution at atomic scale [11].

Provided the cubic crystal system is retained, aliovalent substitution, *e.g.*, with LaF_3 or YF_3, increases the number density of mobile F anions. This effect has been shown for $Ba_{1-x}La_xF_{2+x}$ [25,27]. Starting with SrF_2 and YF_3 (see Fig. 1) a similar behavior is expected. So far, $Sr_{1-x}Y_xF_{2+x}$ solid solutions have been prepared by ceramic synthesis and wet chemical approaches. Here, we report the dynamic parameters of nanocrystalline $Sr_{1-x}Y_xF_{2+x}$ obtained through high-energy ball milling. By using high impact planetary mills we managed to incorporate YF_3 into SrF_2 until the composition $Sr_{0.7}Y_{0.3}F_{2.3}$. Ionic conductivity greatly differs from that of Y-free nanocrystalline SrF_2. Conductivities at elevated temperature might be high enough to realize high-temperature all-solid-state fluorine batteries.

2. Materials and Methods

Nanocrystalline $Sr_{1-x}Y_xF_{2+x}$ samples were prepared in a planetary high-energy ball mill (Fritsch P7, Premium line) by mixing SrF_2 and YF_3 in the desired molar ratio. We used a 45 mL ZrO_2 cub with 140 zirconium oxide milling balls (5 mm in diameter). To guarantee complete transformation the mixtures were milled for 10 h at a rotation speed of 600 rpm under dry conditions, *i.e.*, without the addition of any solvents.

The phase purity and crystal system was checked via X-ray diffractometry (Bruker D8 Advance, Bragg Brentano geometry, 40 kV). With the help of the Scherrer equation we roughly estimated the crystallite size of the samples, see ref. [9,28] for further details on this procedure. Usually, after sufficiently long milling periods the mean crystallite size reaches 10 to 20 nm [29]. ^{19}F magic angle spinning nuclear (MAS) magnetic resonance (NMR) was used to characterize SrF_2 and YF_3 as well as the mixed fluorides at atomic level. We recorded rotor synchronized Hahn echoes by employing a Bruker 2.5-mm MAS probe placed in a 11.4 T cryomagnet. Spectra were measured with a Bruker Avance 500 spectrometer. Spinning was carried out with ambient bearing gas pressure. The $\pi/2$ pulse length was 2.1 μs at 50 W power level; the recycle delay was 20 s and 64 transients were accumulated

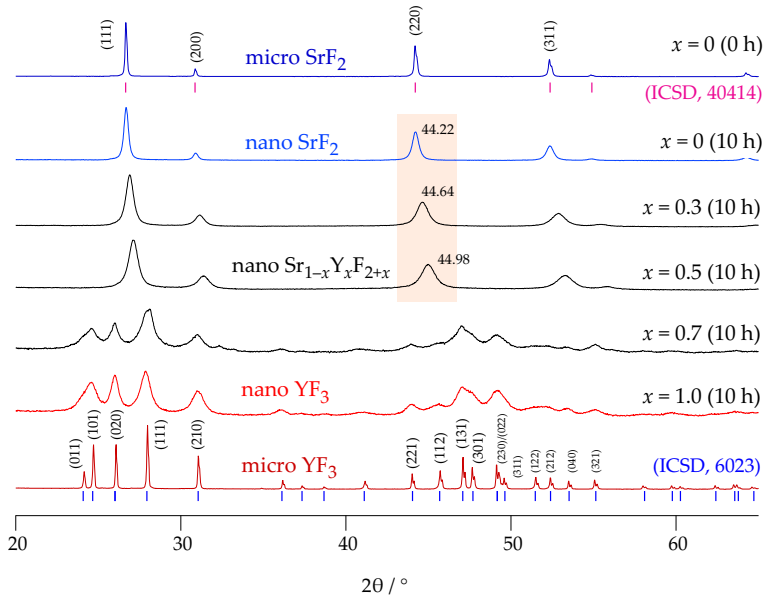

Figure 2. X-ray powder diffractograms recorded ($CuK_{\alpha 1}$, 1.54059 Å) to characterize the phase purity of the starting materials as well as that of the mixed phases formed. The periods indicated in brackets show the milling times. The patterns of microcrystalline SrF_2 and YF_3 perfectly match with those in literature; verticals bars show the average positions of the $CuK_{\alpha 1}$ and $CuK_{\alpha 2}$ reflections. The broadening of the reflections, which is evident for the milled samples, indicates nm-sized crystallites; lattice strain and a distribution of lattice constants due to cation mixing may contribute to the broadening effect seen as well. The equation by Scherrer yields 24(2) nm, 17(2) nm and 15(2) nm as average crystallite size for the samples with $x = 0$, $x = 0.3$ and $x = 0.5$, respectively. Mixing of the cations is anticipated to have a much larger effect on ionic conductivity than the decrease in crystallite size seen for the Y-containing samples.

for each spectrum. We took advantage of LiF powder as a secondary reference $(-204.3$ ppm$)$ [30] to determine chemical shifts δ_{iso}; $CFCl_3$ (0 ppm) served as the primary reference.

To analyze ionic conductivities, the powders were uniaxially cold-pressed to pellets (8 mm in diameter, 0.5 to 1 mm in thickness). After applying electrically conducting Au electrodes (100 to 200 nm) via sputtering, a Novocontrol Concept 80 broadband analyzer was employed to record conductivity isotherms and complex impedances as a function of temperature. The broadband dielectric analyzer was connected to a QUATRO cryo system (Novocontrol) that allows precise settings of temperature and an automatic execution of the measurements. The QUATRO is operated with a stream of freshly evaporated nitrogen gas that passes a heater and enters the sample chamber where the temperature is measured using Pt-100 thermocouples. We used a voltage amplitude of 100 mV and varied the frequency ν from 0.1 Hz to 10 MHz. The isotherms revealed distinct frequency-independent plateaus from which *direct current* DC conductivities σ_{DC} (see above) were read off for each temperature T.

3. Results and discussion

3.1. Structure: X-ray diffraction and ^{19}F high-resolution MAS NMR spectroscopy

Long-range and local structures of $Sr_{1-x}Y_xF_{2+x}$ $(0 \leq x \leq 1)$ were studied by X-ray diffraction and ^{19}F MAS NMR, see Figs. 2 and 3. SrF_2 crystallizes in the cubic crystal system and YF_3 adopts an orthorhombic structure (see Fig. 1). In Fig. 2 the X-ray powder patterns of the starting materials as well as of the milled samples, with the composition $Sr_{1-x}Y_xF_{2+x}$, are shown.

As a result of heavy ball-milling in a planetary mill, the two fluorides form a product with cubic symmetry up to $x = 0.5$. Broadening of the reflections is caused by lattice strain and nm-sized

Preprints (www.preprints.org) | NOT PEER-REVIEWED | Posted: 25 January 2018 doi:10.20944/preprints201801.0234.v1

Peer-reviewed version available at Crystals 2018, 8, 122; doi:10.3390/cryst8030122

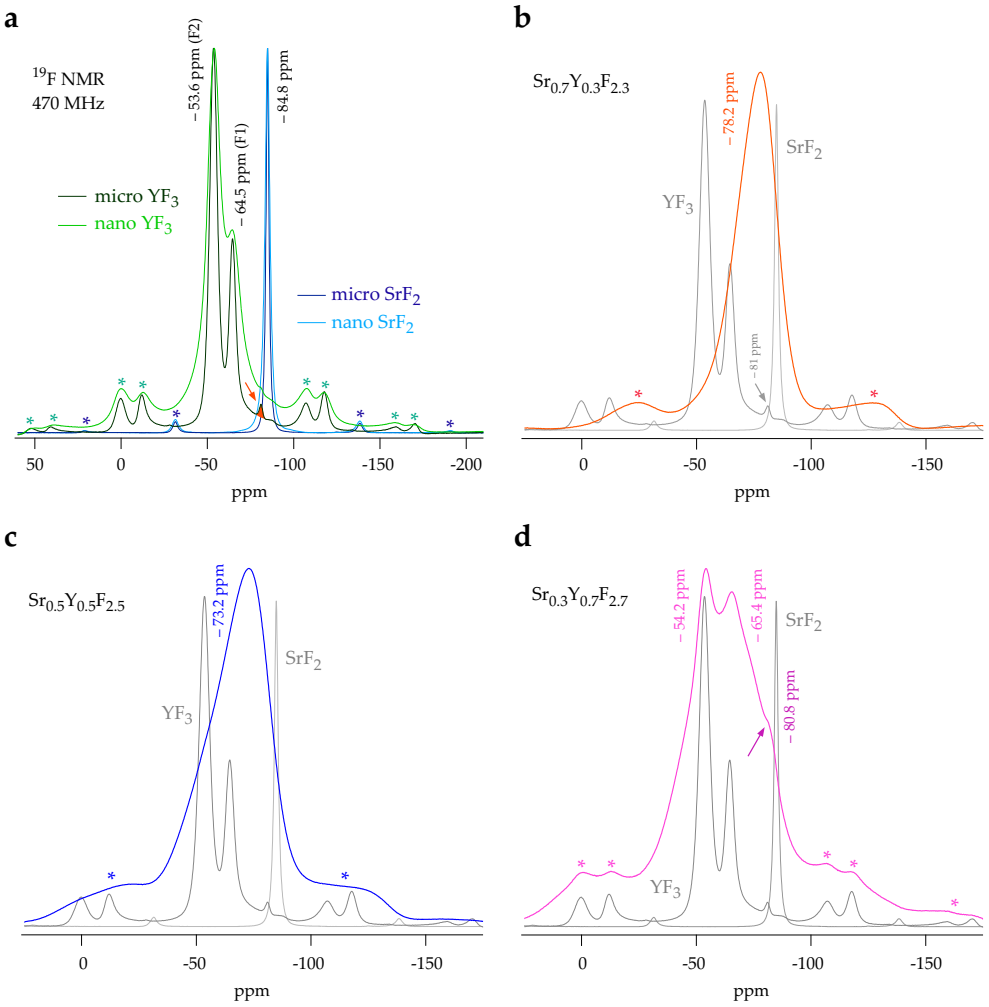

Figure 3. (**a**) to (**d**) ^{19}F MAS NMR spectra of $Sr_{1-x}Y_xF_{2+x}$ prepared by ball milling. We used a rotor-synchronized Hahn echo pulse sequence to record the spectra at a spinning speed of 25 kHz; asterisks $(*)$ denote spinning sidebands. The spectra are referenced to $CFCl_3$ (0 ppm). In (**a**) the spectra of microcrystalline, *i.e.*, unmilled, and nanocrystalline SrF_2 and YF_3 are shown. The nanocrystalline samples were obtained after milling the starting materials for 10 h under dry conditions. Mechanical treatment leads to broadening of the NMR lines because of the defects and polyhedra distortions introduced. The spectra of YF_3 reveal the two magnetically equivalent sites of YF_3; their isotropic chemical shifts δ_{iso} are -53.6 ppm and -84.8 ppm. For the Sr-rich and Y-rich samples, see (**b**) and (**d**), $Sr_{1-x}Y_xF_{2+x}$ with $x = 0.3$ and $x = 0.7$ the center of the broad MAS NMR lines shift toward that of SrF_2 and YF_3, respectively. These shifts, together with the broadening of the lines because of a distribution of chemical shifts caused by atomic disorder, reveals the formation of mixed (Sr,Y) environments the F anions are subjected to. For $x = 0.5$ mixing is most effective, see (**c**).

crystallites. We clearly observe a shift of the reflections toward larger diffraction angles, see the positions of the (220) reflections as indicated in Fig. 2. The lattice constant a gradually changes from 5.8040 Å (SrF_2) to 5.7442 Å ($Sr_{0.7}Y_{0.3}F_{2.3}$). The linear decrease of a, as a result of incorporation of the smaller Y cations, indicates Vegard behaviour. At the same time, F interstitials are generated that are expected to boost F^- ionic conductivity, *vide infra* (Fig. 4).

When coming from pure YF_3, Sr ions are incorporated into the trifluoride. Once again, small crystallites significantly broaden the X-ray reflections; the orthorhombic structure of YF_3 is, however, still conserved. The patterns do not show large amounts of X-ray amorphous material as featureless,

Preprints (www.preprints.org) | NOT PEER-REVIEWED | Posted: 25 January 2018 doi:10.20944/preprints201801.0234.v1

Peer-reviewed version available at Crystals 2018, 8, 122; doi:10.3390/cryst8030122

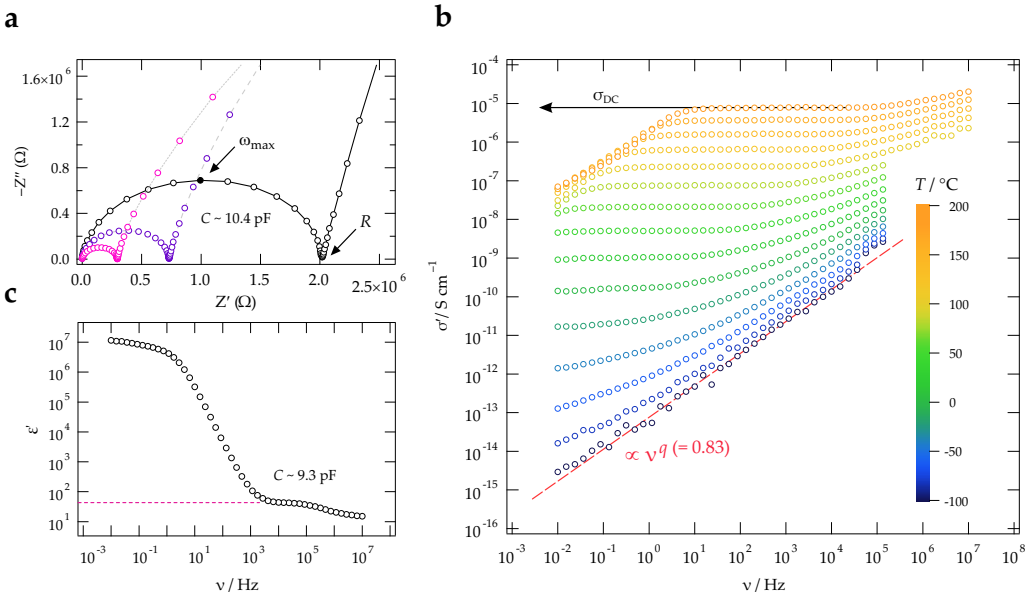

Figure 4. (**a**) Nyquist plots of the complex impedance of $Sr_{1-x}Y_xF_{2+x}$ with $x = 0.3$ recorded at the temperatures indicated. The solid lines are to guide the eye. The depressed semicircles indicate correlated ion movements in the ternary fluoride; from ω_{max} and R capacities, $C = 1/(\omega_{max}R)$, in the order of 10 pF were estimated indicating that the overall electrical response is mainly given by bulk properties rather than grain boundary contributions. (**b**) Conductivity isotherms of $Sr_{0.7}Y_{0.3}F_{2.3}$ recorded from −100 °C to +180 °C in steps of 20 °C. The pronounced plateaus at intermediate frequencies contain the DC conductivity σ_{DC}, as indicated. (**c**) Real part, ϵ', of the complex primitivity as a function of frequency. Above 10^3 Hz the bulk response is seen; the capacity associated with that response is in the order of 10 pF.

broad humps are missing. Hence, we deal with nanocrystalline sample with structurally disordered samples.

Structural disorder is also seen by ^{19}F MAS NMR spectroscopy. In Fig. 3 (a) the spectra of the non-substituted binary fluorides are shown. As expected, coarse grained SrF_2 only shows a single resonance at −84.8 ppm and the spectrum of YF_3 reveals the two crystallographically inequivalent F positions F(1) and F(2). The samples with μm-sized crystallites are composed of sharp lines that perfectly agree with those presented and analyzed in literature [30,31]. Broadening, but no change in isotropic chemical shift, is observed for the samples treated mechanically. YF_3 shows a negligible amount of an impurity phase, see the NMR signal at $\delta_{iso} = -81$ ppm. Upon incorporation of YF_3, the ^{19}F MAS NMR lines drastically broaden because of the introduction of structural disorder, see also [31]. The various Sr-F environments formed as well as the various defects present, including F vacancies and interstitials, result in a broad distribution of ^{19}F NMR chemical shifts. Depending on which cation is the major component in $Sr_{1-x}Y_xF_{2+x}$ the center of the broad lines is either located near the original chemical shifts δ_{iso} of SrF_2 (Fig. 3 (b)) or those of YF_3 (Fig. 3 (d)). For the equimolar solid-solution with $x = 0.5$, the center of the line is in between that of SrF_2 and YF_3. The shoulder near −50 ppm might indicate Y-rich regions or clusters. For a detailed analysis of ^{19}F MAS spectra we refer to [31]. Indeed, ^{89}Y MAS NMR measurements by Ritter *et al.* [31] suggested F clustering taking place in samples with more 10 mol% of Y^{3+}.

In contrast to other solid-solutions, such as $Me_{1-z}Sr_zF_2$ (Me = Ca, Ba; $0 \leq z \leq 1$) and $Ba_{1-z}Ca_zF_2$, line broadening, *i.e.*, the distribution of chemical shifts, is much larger for $Sr_{1-x}Y_xF_{2+x}$. Because of this effect, even under the MAS conditions applied here, we cannot resolve the (Sr,Y) environments as it was possible for the (Ca,Sr) species in cubic $Ca_{1-z}Sr_zF_2$ with a similar range of chemical shifts.

Preprints (www.preprints.org) | NOT PEER-REVIEWED | Posted: 25 January 2018 doi:10.20944/preprints201801.0234.v1

Peer-reviewed version available at Crystals 2018, 8, 122; doi:10.3390/cryst8030122

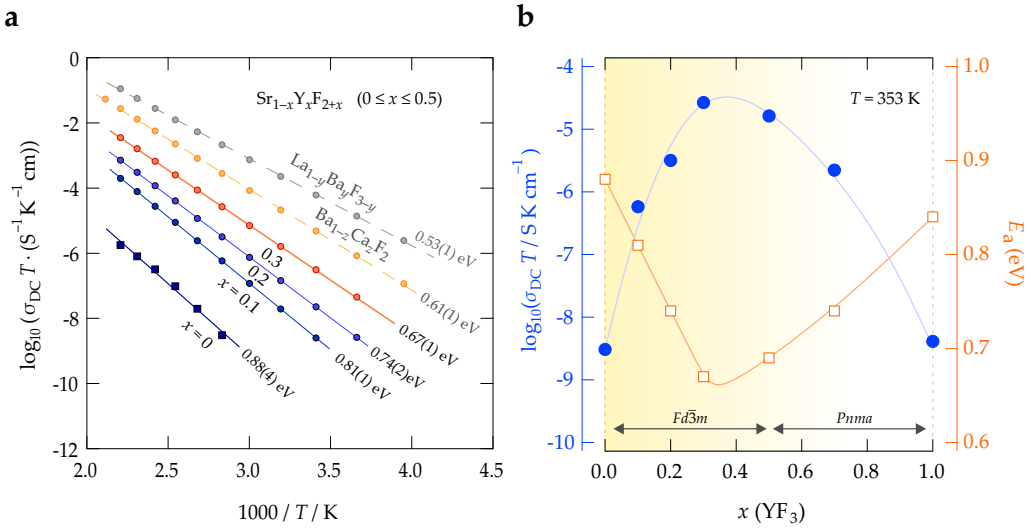

Figure 5. (**a**) Arrhenius plot of $\sigma_{DC}T$ *vs.* the $1/T$ of mechanochemically prepared $Sr_{1-x}Y_xF_{2+x}$. Solid and dashed lines represent fits according to an Arrhenius equation, $\sigma_{DC}T \propto \exp(-E_a/(k_BT))$; k_B denotes Boltzmanns constant. The activation energies obtained are indicated. (**b**) Change of E_a (see right axis) and $\sigma_{DC}T$ of nanocrystalline $Sr_{1-x}Y_xF_{2+x}$ as a function of x.

In Fig. 4 (a) and (b) Nyquist plots and conductivity isotherms of $Sr_{1-x}Y_xF_{2+x}$ with $x = 0.3$ are displayed. Plotting the real part σ' of the complex conductivity $\hat{\sigma}$ results in curves with (i) distinct DC plateaus at sufficiently low frequencies and (ii) a dispersive part at low T and high frequencies. The collapse of σ' at the lowest frequencies and highest temperature is because of F anion charge accumulation in front of the ion-blocking electrode. We used the frequency-independent plateau to determine specific ionic conductivities as a function of temperature. These values refer to long-range ion transport and characterize successful charge displacements in the fluoride. The same values for σ' can be inferred from analyzing Nyquist plots (see Fig. 3 (a)) that show the imaginary part $(-Z'')$ of the complex impedance $\hat{Z}$ as a function of its real part Z'. From the intercept of the semicircle the variable-temperature resistance R can be extracted and converted into σ'. The electrical relaxation process seen in conductivity (or impedance) spectroscopy refers to a bulk process as the corresponding electrical capacity takes values in the pF range, see Fig. 4 (a).

The shape of the isotherms $\sigma'(\nu)$, *cf.* Fig. 4 (b), does not change much with temperature indicating that the same relaxation process is probed at elevated T. At sufficiently high T, the data fulfill the so-called time-temperature superposition principle [32,33]. At low T, however, the dispersive part, which is sensitive to ion dynamics on shorter length scales than those seen in the DC regime, dominates the spectra. This regime can be approximated with Jonscher's power law ansatz, $\sigma'(\nu) \propto \nu^q$ [32]. The exponent q increases with temperature, most likely reaching $q = 1$ at cryogenic temperatures. At such low temperatures localized ion movements might play a rôle that do not contribute to long-range charge transport any longer [34]. The isotherm of $Sr_{0.7}Y_{0.3}F_{2.3}$ recorded at $T = 100\,°C$ is characterized by $q = 0.83(2)$. q values of approximately 0.8 are frequently seen for disordered ion conductors in this T range [25].

In Fig. 5 (a) the product $\sigma_{DC}T$ is plotted *vs.* the inverse temperature $1/T$ to determine activation energies E_a of the samples prepared and to illustrate the change in ionic conductivity upon Y^{3+} incorporation. For comparison, we included the Arrhenius lines of two other mechanochemically prepared F^- anion conductors *viz.* $Ba_{0.5}Ca_{0.5}F_2$ and $La_{0.9}Ba_{0.1}F_{2.9}$. While pure (nanocrystalline) SrF_2 is a poor ionic conductor with an activation energy as high as 0.88 eV; E_a is significantly decreased to 0.67 eV for $Sr_{0.7}Y_{0.3}F_{2.3}$. The ionic conductivity, as well as the activation energy (0.84 eV) of nanocrystalline YF_3 turned out to be very similar to that of nano-SrF_2. In Fig. 5 (b) the change in $\sigma_{DC}T$ and E_a is shown as a function of x. From $x = 0$ to $x = 0.3$ the activation energy almost linearly

decrease; $\sigma_{DC}T$ passes through a maximum at *ca.* $x = 0.3$. Further incorporation of YF_3 causes $\sigma_{DC}T$ to decrease again. Note that the $Sr_{1-x}Y_xF_{2+x}$ system adopts cubic structure up to approximately $x = 0.5$, while the Y-rich samples crystallize with orthorhombic structure. Ultimately, at 80 °C (see Fig. 5 (b)) we notice an enhancement in ionic conductivity by 4 orders of magnitude when going from SrF_2 to $Sr_{0.7}Y_{0.3}F_{2.3}$. This opens the way to systematically vary the ionic conductivity of the ternary fluoride over a broad dynamic range.

Interestingly, already at low Y^{3+} contents, that is, at 10 mol%, we see an increase in ionic conductivity by one order of magnitude. The change in E_a from 0.88 eV to 0.81 eV is accompanied by a significant increase of the pre-exponential factor σ_0 in $\sigma_{DC}T = \sigma_0 \exp(-E_a/(k_BT))$. While $\log(\sigma_0/(\text{S cm}^{-1}\text{K}))$ of SrF_2 amounts to 4.1, it increases to 5.3 for $Sr_{0.9}Y_{0.1}F_{2.1}$. Thus, the new defect structure, most likely involving F clustering as seen by ^{89}Y NMR [31] also influences besides the number of effective charge carriers also attempt frequencies of the underlying jump processes. Most likely, substitution of Sr^{2+} with Y^{3+} will also influence the activation entropy for ionic migration. For $x > 0.1$ no further increase of σ_0 is seen; the additional increase in σ_{DC} is mainly governed by the reduction in activation energy. As the defect concentration is already high in this regime, we expect that predominantly lower migration energies facilitate ion transport further.

4. Conclusions

The mixed system $Sr_{1-x}Y_xF_{2+x}$ represents an attractive system to control ionic conductivities via the concept of cation mismatch. High-energy ball milling is able to force the distinctly sized cations to form a mixed phase with structural disorder at atomic scale. Treating SrF_2 with YF_3 in a high-energy planetary mill causes the original conductivity to increase by some orders of magnitude. Simultaneously, the corresponding activation energy decreases from 0.88 eV to 0.67 eV clearly showing a lowering of the migration barrier the ions have to surmount to take part in long-range transport. Besides this decrease in E_a we also observed the influence of the Arrhenius pre-factor to decisively initiate the boost in ionic transport at $x \leq 0.1$, *i.e.*, in the compositional range where F clustering starts.

Acknowledgments: We thank the Deutsche Forschungsgemeinschaft (DFG) for financial support (SPP 1415).

Author Contributions: S.B., B.S. and M.W. conceived and designed the experiments; S.B., V.P and S.L. performed the experiments; all authors were involved in analyzing and interpreting the data. S.B. and M.W. wrote the paper.

Conflicts of Interest: The authors declare no conflict of interest.

References

1. Tuller, H.L. *Solid State Ion.* **2000**, *131*, 143.
2. Knauth, P. *Solid State Ion.* **2009**, *180*, 911.
3. Kobayashi, S.; Tsurekawa, S.; Watanabe, T. *Beil. J. Nanotechnol.* **2016**, *7*, 1829.
4. Uitz, M.; Epp, V.; Bottke, P.; Wilkening, M. Ion dynamics in solid electrolytes for lithium batteries. *J. Electroceram.* **2017**, *38*, 142.
5. Heitjans, P.; Indris, S. *J. Phys.: Condens. Matter* **2003**, *15*, R1257.
6. Prutsch, D.; Breuer, S.; Uitz, M.; Bottke, P.; Langer, J.; Lunghammer, S.; Philipp, M.; Posch, P.; Pregartner, V.; Stanje, B.; Dunst, A.; Wohlmuth, D.; Brandstütter, H.; Schmidt, W.; Epp, V.; Chadwick, A.; Hanzu, I.; Wilkening, M. *Z. Phys. Chem.* **2017**, *231*, 1361.
7. Heitjans, P. and Masoud, M. and Feldhoff, A. and Wilkening, M.. *Faraday Discuss.* **2007**, *134*, 67.
8. Epp, V.; Wilkening, M. *ChemPhysChem* **2013**, *14*, 3706.
9. Wilkening, M.; Epp, V.; Feldhoff, A.; Heitjans, P. *J. Phys. Chem. C* **2008**, *112*, 9291.
10. Düvel, A.; Ruprecht, B.; Heitjans, P.; Wilkening, M. *J. Phys. Chem. C* **2011**, *115*, 23784.
11. Ruprecht, B.; Wilkening, M.; Steuernagel, S.; Heitjans, P. *J. Mater. Chem.* **2008**, *18*, 5412.
12. Sorokin, N.I.; Buchinskaya, I.I.; Fedorov, P.P.; Sobolev, B.P. *Inorg. Mater.* **2008**, *44*, 189.
13. Maier, J. *Progr. Solid State Chem.* **1995**, *23*, 171.
14. Maier, J. *Nature Mater.* **2005**, *4*, 805.
15. Maier, J. *Z. Phys. Chem. Inter. Ed.* **2003**, *217*, 415.

16. Maier, J. *Phys. Chem. Chem. Phys.* **2009**, *11*, 3011.
17. Puin, W.; Rodewald, S.; Ramlau, R.; Heitjans, P.; Maier, J. *Solid State Ion.* **2000**, *131*, 159.
18. Sata, N.; Eberman, K.; Eberl, K.; Maier, J. *Nature* **2000**, *408*, 946.
19. Jin-Phillipp, N.Y.; Sata, N.; Maier, J.; Scheu, C.; Hahn, K.; Kelsch, M.; Rühle, M. *J. Chem. Phys.* **2004**, *120*, 2375.
20. Vergentev, T.; Banshchikov, A.; Filimonov, A.; Koroleva, E.; Sokolov, N.; Wurz, M.C. *Sci. Techn. Adv. Mater.* **2016**, *17*, 799.
21. Sepelak, V.; Duvel, A.; Wilkening, M.; Becker, K.D.; Heitjans, P. *Chem. Soc. Rev.* **2013**, *42*, 7507.
22. Gleiter, H. *Beil. J. Nanotechnol.* **2013**, *4*, 517.
23. Chadwick, A.V.; Düvel, A.; Heitjans, P.; Pickup, D.M.; Ramos, S.; Sayle, D.C.; Sayle, T.X.T. *IOP Conf. Ser.: Mater. Sci. Engin.* **2015**, *80*, 012005.
24. Preishuber-Pflügl, F.; Wilkening, M. *Dalton Trans.* **2016**, *45*, 8675.
25. Preishuber-Pflügl, F.; Bottke, P.; Pregartner, V.; Bitschnau, B.; Wilkening, M. *Phys. Chem. Chem. Phys.* **2014**, *16*, 9580.
26. Ruprecht, B.; Wilkening, M.; Feldhoff, A.; Steuernagel, S.; Heitjans, P. *Phys. Chem. Chem. Phys.* **2009**, *11*, 3071.
27. Rongeat, C.; Reddy, M.A.; Witter, R.; Fichtner, M. *J. Phys. Chem. C* **2013**, *117*, 4943.
28. Düvel, A.; Wegner, S.; Efimov, K.; Feldhoff, A.; Heitjans, P.; Wilkening, M. *J. Mater. Chem.* **2011**, *21*, 6238.
29. Indris, S.; Bork, D.; Heitjans, P. *J. Mater. Synth. Proc.* **2000**, *8*, 245.
30. Sadoc, A.; Body, M.; Legein, C.; Biswal, M.; Fayon, F.; Rocquefelte, X.; Boucher, F. *Phys. Chem. Chem. Phys.* **2011**, *13*, 18539–18550.
31. Ritter, B.; Krahl, T.; Scholz, G.; Kemnitz, E. *J. Phys. Chem. C* **2016**, *120*, 8992.
32. Dyre, J.C.; Maass, P.; Roling, B.; Sidebottom, D.L. *Rep. Progr. Phys.* **2009**, *72*, 046501.
33. Sakellis, I. *Appl. Phys. Lett.* **2011**, *98*, 072904.
34. Funke, K.; Cramer, C.; Wilmer, D. 2nd ed.; Springer, Berlin; ed. by P. Heitjans, J. Kärger, 2005; chapter 21, pp. 857–893.

Sample Availability: Samples of the compounds mentioned in this study are available from the authors.